ACCSCIENCE PUBLISHING

International Journal of Bioprinting

RESEARCH ARTICLE

3D-printed dual-crosslinked hydrogel scaffold loaded with ginger-derived exosomes for enhanced infected wound healing

Shuhao Yang[1†], Yidong Shen[1,2†], Haoming Wu[3†], Jixin Zhou[3], Yingying Chen[3], Jiayu Liu[3], Yixuan Lan[3], Kaichen Shen[1], Wei Huang[1*], Leilei Qin[1*], and Hai Wang[4*]

[1]Department of Orthopaedic Surgery, Chongqing Municipal Health Commission Key Laboratory of Musculoskeletal Regeneration and Translational Medicine/Orthopaedic, Chongqing Medical University, Chongqing 400010, China

[2]Department of Orthopaedics, Yancheng First Hospital, Affiliated Hospital of Nanjing University Medical School, Yancheng, Nanjing 210006, China

[3]School of Preclinical Medicine of Chengdu University, Clinical Medical College and Affiliated Hospital of Chengdu University, Chengdu University, Sichuan 610106, China

[4]Department of Orthopaedics, Chongqing University Fuling Hospital, Chongqing 400044, China

[†]*These authors contributed equally to this work.*

***Corresponding authors:**
Hai Wang
(wanghai9022@sina.com)
Leilei Qin
(253505921@qq.com)
Wei Huang
(huangwei68@263.net)

Citation: Yang S, Shen Y, Wu H, *et al*. 3D-printed dual-crosslinked hydrogel scaffold loaded with ginger-derived exosomes for enhanced infected wound healing. *Int J Bioprint.* 2026;12(3):026090080. doi: 10.36922/IJB026090080

Received: February 28, 2026

Revised: April 13, 2026

Accepted: April 24, 2026

Published online: May 1, 2026

Abstract

Infected wounds pose a significant clinical challenge, as persistent bacterial colonization exacerbates inflammation, disrupts the local immune microenvironment, and delays tissue repair. Here, we report the development of a 3D printing dual-crosslinked hydrogel scaffold loaded with ginger-derived exosome-like vesicles (GPP@G-ELNs) to promote healing of infected full-thickness wounds. The hydrogel was fabricated by combining GelMA-PBA and PVA to form a dual-network structure, followed by photo-crosslinking and 3D printing, and then loaded with G-ELNs. The bioactivity of the scaffold was evaluated in an infected rat wound model, focusing on wound closure, angiogenesis, antibacterial efficacy, and immunomodulatory effects. Treatment with GPP@G-ELNs hydrogel significantly accelerated wound healing, reduced inflammatory cell infiltration, promoted collagen deposition, and enhanced angiogenesis. Moreover, the hydrogel exhibited potent antibacterial activity, with ginger-derived exosomes playing a critical role in modulating macrophage polarization and controlling local immune responses. These findings demonstrate that the 3D printing GPP@G-ELNs hydrogel provides an integrated platform for infection control, immunoregulation, and tissue regeneration, offering promising potential for clinical application in the management of infected wounds.

Keywords: Infected wound healing; 3D printing; Dual-crosslinked hydrogel; Exosomes; Infection control

1. Introduction

Infected wounds are a common and challenging clinical problem, as persistent bacterial colonization exacerbates inflammation, disrupts the local immune microenvironment, and impairs angiogenesis, ultimately delaying tissue repair and compromising patient

outcomes.[1,2] Such wounds often arise in the context of underlying conditions, including diabetes and peripheral vascular disease, which further compromise local blood supply and immune function, making the infection difficult to control and the healing process prolonged. In recent years, hydrogels have gained widespread attention in wound healing due to their excellent biocompatibility, high water content, and drug-loading capacity.[3,4] However, most traditional hydrogels rely on permanent crosslinking structures to maintain their integrity. Once they break, rupture, or locally fail in the dynamic environment of a wound, they are typically unable to spontaneously restore their structure and function.[5] During wound healing, the wound undergoes repeated stretching, compression, and external mechanical stimulation, making hydrogels, which lack self-healing capabilities, prone to structural damage, incomplete coverage, or detachment, resulting in disrupted drug release or loss of antimicrobial barriers,[6,7] severely limiting their long-term therapeutic effects.[8] Therefore, developing a hydrogel capable of maintaining structural integrity and functional stability under repeated mechanical disturbances and complex pathological microenvironments is of great significance for achieving sustained infection control and dynamic repair.

Self-healing hydrogels, with their excellent injectability and *in situ* gelation properties, allow for tight adhesion to wounds and support dynamic healing, making them a promising direction in wound healing research.[9] Lu *et al.*[10] developed a hyaluronic acid-based hydrogel loaded with peptides, which effectively adhered to wounds and promoted tissue regeneration. Tan *et al.*[11] used dynamic imine-bond crosslinking among hydroxypropyl chitosan (HPC), caffeic acid-modified chitosan (CCS), and oxidized dextran (ODex) to create a sprayable chitosan-based hydrogel for in situ wound repair. Furthermore, the photopolymerizable hydrogels such as methacrylated gelatin (GelMA) demonstrate the advantage of ease of operation and can be modified with substances like phenylboronic acid (PBA) to achieve dynamic responses to factors such as reactive oxygen species (ROS) and pH in the wound microenvironment.[12] Although these self-healing injectable hydrogels show significant advantages in adhering to irregular wound shapes and facilitating dynamic healing, their structures are typically uniform and disordered, making it difficult to control their mechanical properties and spatial structures precisely.[13] During actual wound healing, the wound is often exposed to dynamic forces such as stretching, compression, and external mechanical disturbances.[14] Relying solely on injectable hydrogels can lead to local collapse, deformation, or functional degradation, thus limiting their long-term efficacy. In contrast, hydrogels fabricated using 3D printing technology can maintain their self-healing properties while offering controllable and repeatable design of macroscopic shape, pore structure, and mechanical performance.[15] By precisely controlling the printing path and structural parameters, 3D printing hydrogels can better adapt to various wound shapes and provide stable mechanical support at the structural level, making them more effective in addressing the dynamic mechanical environment of wound healing.[16] This advantage gives 3D printing self-healing hydrogels greater potential for application in complex wound repair.

In the clinical treatment of infectious wounds, antibiotics remain the primary method for controlling bacterial infections.[17] However, the long-term or repeated use of antibiotics not only increases the risk of bacterial resistance but may also have toxic effects on local cell activity, inhibiting the proliferation and migration of fibroblasts and endothelial cells, thereby negatively impacting the wound-healing process.[18] In recent years, bioactive compounds derived from natural plants have gained significant attention due to their excellent biological safety, low cost, and multitarget regulatory properties in infection control and immune modulation.[19] As a commonly used food and medicinal plant, ginger is rich in various bioactive components that have been shown to possess antibacterial, anti-inflammatory, and immune-regulating functions, demonstrating potential advantages in infection control and the treatment of inflammation-related diseases.[20] Compared with single chemical drugs, plant-derived bioactive substances generally exert milder and more durable biological effects, rendering them more suitable for highly sensitive scenarios such as wound healing. Among these, exosome-like nanovesicles (ELNs) extracted from fresh plant juice are membranous aggregates composed of lipids, proteins, nucleic acids and other biomolecules, and possess pharmacological activities similar to those of the source plants. In contrast to single-component agents, ELNs are characterized by multi-component composition, cross-scale structural features and multifunctional biological effects, exhibiting distinct advantages in cellular uptake, multivalent interactions and functional synergy.[21] Furthermore, compared with mammalian exosomes, ELNs are naturally devoid of mammalian antigens, thus presenting lower immunogenicity and reduced risk of pathogen transmission.[22]

In this study, we developed a 3D printing dual-crosslinked hydrogel scaffold (GPP@G-ELNs) loaded with ginger-derived exosome-like nanovesicles (G-ELNs). This system combines phenylboronic acid-modified methacrylated gelatin (GelMA-PBA) with polyvinyl alcohol (PVA) to construct a dual-crosslinked hydrogel

network. The composite hydrogel system maintains structural stability while possessing self-healing ability to dynamically respond to wound movement and exhibits responsive degradation and drug release capabilities in the pathological microenvironment rich in ROS. Additionally, the G-ELNs loaded in the GPP hydrogel can effectively eliminate pathogenic bacteria and regulate the local immune microenvironment. In a full-thickness infectious wound model, the GPP@G-Exo hydrogel significantly accelerated the wound healing process and demonstrated pro-angiogenic and anti-inflammatory effects. In summary, this 3D printing dual-network drug-loaded hydrogel provides a promising functional material platform for skin tissue repair in infectious wounds and holds great application potential.

2. Materials and methods

2.1. Materials

Gelatin (medical grade, Bloom 240), methacrylic acid (MAA), boric acid salts, and polyvinyl alcohol (PVA) were purchased from Aladdin Reagents Co., Ltd. (Shanghai, China). The photoinitiator Irgacure 2959 (2-(hydroxy)-4-(2-hydroxyethoxy)-2-methylphenyl ketone) was obtained from Sigma-Aldrich (St. Louis, USA). 1-Ethyl-3-(3-dimethylaminopropyl) carbodiimide hydrochloride (EDC) and N-hydroxysuccinimide (NHS) were purchased from TCI Chemicals (Shanghai, China). All chemicals were of analytical grade and were used without further purification, unless otherwise specified.

2.2. Synthesis of GelMA-PBA hydrogel

GelMA was synthesized following the conventional preparation method. In brief, gelatin was dissolved in phosphate-buffered saline (PBS) and methacrylic acid (MAA) was added. The mixture was treated at 50 °C for 6 h, then placed into a dialysis bag and dialyzed in deionized water at 37 °C for 3 days, followed by freeze-drying for 2 days. For the synthesis of GelMA-PBA, the freeze-dried GelMA was dissolved in 50 mL PBS at a concentration of 5% w/v and the pH was adjusted to 5.5–6.0. Then, equimolar amounts of EDC and NHS were added and activated at room temperature for 30 min. Next, 1 g of amino phenylboronic acid hydrochloride was added and the pH was adjusted to 6.0–6.5, followed by continued reaction for 12–24 h (stirred in the dark at room temperature). After the reaction, the product was transferred to a dialysis bag (MWCO 3.5–8 kDa) and dialyzed in deionized water for 3–5 days (with water changes 2–3 times per day) to remove unreacted small molecules and by-products. The product was then freeze-dried to obtain GelMA-PBA powder for later use.

2.3. Synthesis and characterization of GPP hydrogel

GelMA-PBA and PVA were mixed to construct a composite hydrogel (GPP). GelMA-PBA and PVA were each dissolved in PBS solution containing the photoinitiator Irgacure 2959 at a concentration of 10% w/v. The two solutions were then mixed at volume ratios of 8:2, 6:4, and 4:6 to form the pre-crosslinked hydrogel system. Under slightly alkaline conditions (pH ≈ 8.5), a reversible borate ester dynamic covalent reaction was induced in the hydrogel. The pre-crosslinked hydrogel was then exposed to ultraviolet light (365 nm, approximately 30 mW/cm^2) for photo-crosslinking, which induced free radical polymerization of the methacrylate groups on the GelMA backbone, forming a stable dual-crosslinked composite hydrogel. The composite hydrogel was characterized by Fourier-transform infrared spectroscopy (FTIR), proton nuclear magnetic resonance spectroscopy (^{1}H NMR), and scanning electron microscopy (SEM) to systematically analyze its chemical structure, component interactions, and micromorphology. FTIR analysis was performed using a Nicolet iS50 spectrometer (Thermo Fisher Scientific, USA), with spectra collected in the range of 4000–400 cm^{-1}. For ^{1}H NMR measurements, a Thermo Fisher Scientific NMR System 400 MHz spectrometer (Thermo Fisher Scientific, USA) was employed. The lyophilized hydrogel was dissolved in deuterated dimethyl sulfoxide (DMSO-d_6) to confirm the chemical structure of the hydrogel and verify the successful integration of each component. SEM observation was carried out on a Thermo Fisher Scientific Phenom ProX SEM (Thermo Fisher Scientific, USA). The samples were sputter-coated with a 5-nm-thick gold layer, and images were acquired at an accelerating voltage of 10 kV to observe the surface and cross-sectional morphology as well as the pore size distribution of the hydrogel.

For the swelling experiment, GPP hydrogels with different ratios were prepared into cylindrical samples of the same size (*e.g.*, diameter d, height h; $n \geq 3$ for each group). After gelation, the samples were thoroughly washed with PBS to remove unreacted small molecules and residual initiators, then freeze-dried to constant weight, and the dry weight (Wd) was recorded. The freeze-dried samples were placed in PBS at pH 7.4 and incubated at 37 °C with shaking. At preset time points, the samples were taken out, surface liquid was gently absorbed with filter paper, and the wet weight (Ws) was measured. The swelling ratio of the hydrogel was calculated using the following formula:

$$\text{Swelling ratio (\%)} = \frac{\text{Ws} - \text{Wd}}{\text{Wd}} \times 100$$

For the hydrogel degradation experiment, GPP hydrogels were prepared into samples of the same size (n

≥ 3 for each group) and freeze-dried to constant weight, recording the initial dry weight as W0. The samples were then placed in centrifuge tubes containing pH 7.4 PBS and incubated at 37 °C with shaking, with regular PBS changes to maintain a stable degradation environment. At preset time points, the samples were removed, gently rinsed with deionized water to remove surface salts, then freeze-dried to constant weight, and the remaining dry weight (Wt) was recorded. The mass loss rate of the hydrogel was calculated using the following formula:

$$\text{Mass loss (\%)} = \frac{W0 - Wt}{W0} \times 100$$

2.4. Synthesis and characterization of G-ELNs

Fresh ginger was thoroughly washed in sterile PBS solution and processed under sterile conditions. The tissue was homogenized in a sterilized blender using pre-cooled sterile PBS (pH 7.4) to minimize thermal and environmental contamination. The homogenate was then filtered through sterile gauze to remove fibrous impurities, followed by differential centrifugation at 4 °C (300× *g* for three short cycles and 10,000× *g* for 30 min) to remove large particles and residual impurities. The supernatant was filtered through a 0.22 μm polyethersulfone membrane filter and subjected to ultracentrifugation at 100,000× *g* for 60 min at 4 °C (using a Beckman Coulter centrifuge). The final pellet was gently resuspended in PBS and characterized using transmission electron microscopy (TEM) to assess vesicle morphology and nanoparticle tracking analysis (NTA) to determine particle size distribution. In addition, the protein composition of the purified ginger-derived exosome-like nanoparticles was evaluated by sodium dodecyl sulfate-polyacrylamide gel electrophoresis (SDS-PAGE), providing a protein profile characteristic of exosome-like vesicles. The vesicles were aliquoted and stored at −80 °C until further use.

2.5. 3D printing of GPP@G-ELNs hydrogel scaffold

The scaffolds were fabricated using an extrusion-based 3D bioprinter. Briefly, the GelMA-PBA, PVA, and G-Exo solution was thoroughly mixed and cooled at 4 °C for 20 min. The bioink was then loaded into the printer nozzle, with a 22G needle and a layer thickness of 0.8 mm. The extrusion temperature was maintained at 4 °C to preserve the gel state, and the bioink was extruded under a pressure of 20–50 kPa at a speed of 5.0 mm/s. The printing temperature was controlled between 5 °C and 15 °C, with the cooling plate maintained at −4 °C. After printing, the scaffolds were crosslinked under ultraviolet (UV) irradiation on the cooling plate and subsequently lyophilized for characterization.

2.6. Mechanical strength testing

The mechanical properties of the hydrogel scaffold were evaluated through compression and tensile tests using a universal testing machine. For the compression test, cylindrical hydrogel samples (10 mm in diameter and 4 mm in height) were placed between parallel compression plates and subjected to uniaxial compression at a loading rate of 10 mm/min to obtain the compressive stress–strain curve. For the tensile test, dumbbell-shaped hydrogel samples were tested in the same manner, with a stretching rate of 10 mm/min until fracture, and the tensile stress–strain curve was recorded. All samples were fully equilibrated in PBS (pH 7.4) before testing and tested under wet conditions. Each experiment was repeated at least three times.

2.7. Drug release experiment

To evaluate the release behavior of exosomes from the hydrogel scaffold, the exosome-loaded hydrogel samples were placed in 1 mL of PBS (pH 7.4) and incubated at 37 °C. At predetermined time points, the supernatant was collected and replaced with an equal volume of fresh PBS to maintain a constant volume in the release system. The collected supernatants were analyzed using a UV-Vis spectrophotometer, and the absorbance at 280 nm was measured to reflect the release of exosome-related proteins.

2.8. Hemolysis test

The blood compatibility of the materials was assessed using whole blood from Sprague–Dawley (SD) rats. Freshly collected whole blood was anticoagulated with 3.2% w/v sodium citrate and centrifuged at 2000 rpm for 10 min at room temperature to separate the red blood cells. After discarding the supernatant plasma, the red blood cells were washed three times with PBS until the supernatant became clear. The red blood cells were then resuspended in PBS and diluted to a 5% v/v red blood cell suspension. A 500 μL aliquot of the red blood cell suspension was mixed with an equal volume of deionized water (positive control), PBS (negative control), GPP hydrogel, and GPP@G-ELNs hydrogel, and incubated at 37 °C for 4 h. After incubation, the mixture was centrifuged at 2000 rpm for 10 min, and the supernatant was collected for hemolysis analysis.

2.9. Cytotoxicity

To obtain standardized hydrogel extracts, the formed hydrogels were initially sterilized by soaking in 75% ethanol under sterile conditions at 75 °C for 30 min. Afterward, the hydrogels were thoroughly washed three times with sterile PBS to remove residual ethanol. The treated hydrogels were then placed in sterile cell culture medium (DMEM containing 10% FBS and 1% penicillin-streptomycin) at a mass/volume ratio of 0.1 g/mL, and incubated at 37 °C with

5% CO_2 for 24 h to extract the hydrogel. After extraction, the supernatant was collected and filtered through a 0.22 μm sterile filter, and the resulting filtrate was used as the hydrogel extract for subsequent cell experiments.

The impact of the hydrogel materials on cell viability was assessed using the Cell Counting Kit-8 (CCK-8, Beyotime, China). L929 fibroblasts were seeded at a density of 5×10^4 cells/well in a 96-well plate (100 μL/well) and cultured at 37 °C with 5% CO_2 for 24 h to allow cell adhesion. The culture medium was then discarded, and 100 μL of the pre-prepared hydrogel extract was added to the wells. The control group received an equal volume of fresh DMEM culture medium. After an additional 24 h of incubation, the medium was replaced with fresh culture medium containing 10% v/v CCK-8 reagent (100 μL per well), and the plate was incubated in the dark for 2 h. The absorbance was recorded at 450 nm using a multifunctional microplate reader (Infinite F200/M200, Tecan, Männedorf, Switzerland) to measure cell viability.

To further visually assess cell viability, Live/Dead cell viability staining was performed using a Live/Dead cell staining kit. L929 cells were seeded in a 24-well plate at the same density and treated with hydrogel extracts as described. After treatment, the culture medium was discarded, and the cells were gently washed once with PBS. The staining solution containing calcein-AM and propidium iodide (PI) was added, and the cells were incubated at 37 °C in the dark for 15–20 min. After staining, the cells were gently washed with PBS and observed under a fluorescence microscope. Live cells exhibited green fluorescence, while dead cells exhibited red fluorescence.

2.10. Cell proliferation assay

Cell proliferation was assessed using the CCK-8 assay (Abmole) and the EdU Cell Proliferation Kit with Alexa Fluor 488 (Beyotime) according to the manufacturer's instructions. For the CCK-8 assay, L929 cells were seeded at a density of 5×10^3 cells per well in a 96-well plate and cultured for 1–5 days. At each time point, 10 μL of CCK-8 solution was added to each well, incubated at 37 °C for 2 h, and absorbance was measured at 450 nm using a microplate reader. For the EdU assay, L929 cells were seeded at 5×10^3 cells per well, cultured for 12 h, and then treated with EdU (10 μM) for an additional 12 h. The cells were subsequently fixed, permeabilized, blocked, and stained according to the kit protocol. Images were captured using an inverted fluorescence microscope (DMi8, Leica, Germany), and the proportion of EdU-positive cells was quantified using ImageJ software.

2.11. Antibacterial activity

The antibacterial activity of the hydrogel extract was evaluated in vitro using *Staphylococcus aureus* (*S. aureus*) and *Escherichia coli* (*E. coli*) as representative strains. The prepared hydrogel samples were extracted at 37 °C for 24 h, and the supernatant was collected as the hydrogel extract for further use. After culturing the bacteria to the logarithmic growth phase, the bacterial suspension was diluted to approximately 5×10^4 cfu/mL with sterile buffer. A certain volume of the hydrogel extract was mixed with the bacterial suspension and incubated at 37 °C with shaking at 220 rpm for 8–10 h. The control group consisted of an equal volume of buffer and bacterial suspension co-cultured under the same conditions. After incubation, bacterial growth was evaluated by measuring the optical density of the bacterial suspension at 600 nm, and bacterial survival or inhibition rates were calculated using the formula.

To further visually observe bacterial survival, bacterial samples treated with the extract were stained using a calcein-AM/PI Live/Dead staining kit, following the instructions and incubated in the dark. The stained bacterial samples were imaged using a laser scanning confocal microscope. Live bacteria appeared as green fluorescence, while dead bacteria showed red fluorescence, providing a comprehensive assessment of the antibacterial effect of the hydrogel extract.

2.12. Macrophage polarization

Immunofluorescence staining was used to evaluate the regulatory effects of the hydrogel extract on macrophage inflammatory phenotypes. RAW264.7 cells were seeded at a density of 1×10^5 cells/well in a 24-well plate and cultured overnight at 37 °C with 5% CO_2 to allow cell adhesion. The cells were then pre-stimulated with lipopolysaccharide (LPS, 1 μg/mL) for 4 h. After discarding the culture medium, the cells were gently washed once with PBS and treated with the hydrogel extract; the control group was treated with an equal volume of fresh complete culture medium. After 24 h of incubation, the culture medium was discarded, and the cells were washed twice with PBS. For immunofluorescence analysis, the cells were fixed with 4% paraformaldehyde for 15 min, permeabilized with 0.1% Triton X-100 for 10 min, and blocked with 5% BSA at room temperature for 1 h. The cells were then incubated overnight at 4 °C with primary antibodies against CD86 (M1 marker) and CD206 (M2 marker). Following three washes with PBS, fluorescence-labeled secondary antibodies were added and incubated in the dark for 1 h. Finally, the cells were counterstained with DAPI for 5 min, washed with PBS, and mounted.

Samples were observed under a fluorescence microscope, and CD86- and CD206-positive signals were used to assess changes in M1 and M2 macrophage phenotypes, respectively. Additionally, quantitative polymerase chain reaction (qPCR) analysis was performed to quantify the expression of macrophage-associated inflammatory cytokines, including IL-6 and TNF-α (M1 markers) and IL-10 (M2 marker), to further evaluate the hydrogel's effects on macrophage polarization and the modulation of the inflammatory microenvironment.

2.13. Infectious skin injury model

All animal experiments were conducted in accordance with the "Regulations on the Administration of Laboratory Animals" issued by the Ministry of Health of the People's Republic of China and were approved by the Ethics Committee of Chongqing Medical University. SD rats (5–6 weeks old, 200–250 g) were purchased from Sichuan Dashuo Animal Research Center. After anesthesia, the back hair of each rat was shaved and disinfected, and a circular full-thickness skin wound (10 mm in diameter) was made using surgical scissors. A suspension of *S. aureus* (5×10^8 CFU/mL) was inoculated onto each wound. After 24 h, the wounds were treated with GPP and GPP@G-ELNs hydrogels, while the blank control group received a simple full-thickness skin wound. All wounds were covered with a three-layer sterile gauze and fixed with an elastic bandage and a rubber ring. Wound images were taken on days 0, 7, and 14, and tissue samples were collected and analyzed from 3 rats per group at each time point.

2.14. Histological and immunohistochemical analysis

Rats were euthanized on the 14th day post-surgery, and corresponding tissue samples were immediately fixed in 4% paraformaldehyde for 24 h. After fixation, the tissue samples were dehydrated through a gradient of ethanol, cleared in xylene, and embedded in paraffin. Continuous sections, approximately 4 μm in thickness, were cut and mounted on glass slides for subsequent histological and immunohistochemical analysis. To assess overall tissue morphology, inflammation, and repair, the sections were stained with hematoxylin and eosin (H&E; Solarbio, G1120, China) to observe cell infiltration, tissue structure integrity, and new tissue formation. Masson's trichrome staining was also performed using commercially available kit (Solarbio, G1340, China) to evaluate collagen deposition and tissue remodeling.

Furthermore, to analyze molecular events related to tissue repair, the sections were subjected to immunohistochemical staining to detect the expression of vascular endothelial growth factor (VEGF), type I collagen (COL-1), and tumor necrosis factor-α (TNF-α). Briefly, the paraffin sections were dewaxed and rehydrated, followed by antigen retrieval. Endogenous peroxidase activity was blocked using 3% hydrogen peroxide, and non-specific binding sites were blocked with 5% bovine serum albumin. The sections were incubated overnight at 4 °C with the corresponding primary antibodies. After washing with PBS, HRP-conjugated secondary antibodies were applied for incubation, followed by DAB staining and counterstaining with hematoxylin. All stained sections were observed and imaged using an optical microscope. H&E and Masson's trichrome staining were used for qualitative assessment of tissue morphology, inflammation, and collagen deposition, while the expression of VEGF, COL-1, and TNF-α reflected angiogenesis, matrix remodeling, and the level of inflammation.

2.15. Statistical analysis

Data are presented as the mean ± standard deviation (SD) of at least three independent replicates. Statistical analyses were performed using GraphPad Prism 9 software. Statistical significance was determined using Student's *t*-test or one-way analysis of variance (ANOVA), followed by Tukey's multiple comparisons test. Differences were considered statistically significant at $^{*}p < 0.05$, $^{**}p < 0.01$, $^{***}p < 0.001$, and $^{****}p < 0.0001$. "ns" indicates no significant difference.

3. Results and discussion

3.1. Construction and characterization of GPP hydrogel

In the application of traditional hydrogel dressings, dynamic mechanical changes in the wound area, caused by factors such as limb movement and tissue swelling, often lead to the rupture or detachment of the dressing, exposing the wound and negatively affecting the healing process.[23] In contrast, dynamic hydrogels demonstrate clear advantages in terms of adhesion to the wound interface and mechanical adaptability. By grafting borate ester dynamic covalent bonds onto GelMA hydrogels, the hydrogel network is endowed with reversible crosslinking and stress-adaptive capabilities, while maintaining the excellent biocompatibility and operability of GelMA. Further, by combining with PVA, a dynamic network structure based on borate ester-diol interactions is constructed, thus enabling the reversible self-healing properties of the hydrogel (Figure 1A). The chemical structure of GelMA-PBA was characterized using ^{1}H NMR (Figure 1B). In the ^{1}H NMR spectrum, the characteristic peaks at $\delta \approx 5.3$ ppm and 5.5–5.7 ppm correspond to the vinyl protons ($-CH_2=$) of the methacrylate group, indicating successful grafting of the methacrylate group

onto the GelMA backbone, which is a typical feature of GelMA. Additionally, a new aromatic proton characteristic peak at δ ≈ 7.3–7.8 ppm, corresponding to the phenyl ring protons in the phenylboronic acid (PBA) structure, further confirms the successful introduction of the PBA group into the GelMA backbone. These results indicate that the GelMA-PBA, containing both methacrylate and boronic acid groups, has been successfully synthesized. The chemical structure of GelMA-PBA, PVA, and their composite hydrogel was further characterized using FTIR (Figure 1C). In the FTIR spectrum of GelMA-PBA, the characteristic absorption peaks at approximately 1655 cm^{-1} and 1540–1555 cm^{-1} correspond to the amide I band (C=O stretching vibration) and amide II band (N–H bending vibration), respectively. Additionally, the characteristic absorption peaks at around 1635–1640 cm^{-1} and 1050–1060 cm^{-1}, associated with the methacrylate group, correspond to the C=C stretching vibration and the C=C–H in-plane bending vibration, further confirming the successful introduction of the methacrylate group into the GelMA backbone. For PVA, the FTIR spectrum exhibits a broad and strong absorption band at 3200–3400 cm^{-1}, corresponding to the –OH stretching vibration, and a characteristic peak at approximately 1090 cm^{-1}, corresponding to the C–O stretching vibration.

To screen for the optimal composite hydrogel formulation suitable for wound repair, the swelling behavior and *in vitro* degradation of hydrogels with different GelMA-PBA/PVA ratios were systematically compared (Figure 1D and 1E). The results showed that in the swelling test, the GelMA-PBA/PVA hydrogel with an 8:2 ratio exhibited the highest swelling ratio (up to 534 ± 35.56%) within 120 min, while excessively high swelling often weakens the adhesion stability between the hydrogel and the wound tissue. Further degradation experiments revealed that the composite hydrogel with a 4:6 ratio had the slowest degradation rate, with only about 45.3 ± 3.88% degradation over 14 days, demonstrating higher structural stability. However, an overly slow degradation process may be difficult to match with the wound healing timeline. Considering the balance between swelling behavior, structural stability, and biodegradability, the GelMA-PBA/PVA 6:4 ratio GPP hydrogel was ultimately selected for subsequent experiments.

3.2. Self-healing and dynamic response performance of GPP hydrogel

The microstructure of GelMA-PBA, PVA, and GPP hydrogels was studied using SEM (Figure 1F). The results showed that PVA hydrogel exhibited a characteristic porous structure, while GelMA-PBA hydrogel had larger circular pore sizes. Furthermore, the pores of the GPP hydrogel combined the characteristics of both hydrogels, confirming the successful composite formation of the hydrogel. The gelation performance of the hydrogels was preliminarily evaluated using a tilting experiment. As shown in Figure 1G, individual GelMA-PBA or PVA systems displayed noticeable flow under tilting conditions, while the composite hydrogel maintained a stable gel shape under gravity, indicating the formation of effective borate ester dynamic covalent bonds within the system, thus constructing a stable three-dimensional network structure.

Further, different dyeing methods were applied to the hydrogels (Figure 1H), and the hydrogels were physically cut and reassembled to evaluate their self-healing ability. The results showed that hydrogels of different colors quickly fused into a whole after being cut and brought back together, and maintained their structural integrity during subsequent handling, fully demonstrating the excellent self-healing performance of the composite hydrogel.

The borate ester dynamic covalent bonds not only imparted good self-healing properties to the hydrogel, but their unique ROS-responsive characteristics also allowed the hydrogel to selectively respond to the ROS enriched in the infectious microenvironment, enabling controllable degradation. To verify this characteristic, GPP hydrogel samples were treated with H_2O_2 and PBS, and an inverted experiment was conducted (Figure 1I). The results showed that the GPP hydrogel treated with H_2O_2 exhibited significant structural damage and gradually dissolved, while the PBS-treated group remained stable under the same conditions. Further *in vitro* degradation results showed that, within 8 days, the mass loss rate of the GPP hydrogel in the H_2O_2-treated group exceeded 80% (Figure 1J). This significant ROS-responsive degradation behavior is primarily attributed to the ROS-induced cleavage of borate ester bonds, which disrupts the dynamic crosslinking network inside the hydrogel, ultimately leading to the accelerated disintegration of the gel.[24]

3.3. Synthesis and characterization of 3D-printed GPP@G-ELNs

To construct an integrated hydrogel capable of regulating the infectious wound microenvironment, exosome-like nanovesicles were first extracted from ginger (G-ELNs) (Figure 2A). TEM results demonstrated that the extracted G-ELNs exhibited a typical bilayer spherical structure (Figure 2B). The particle size of G-ELNs was analyzed by NTA (Figure 2C), revealing a primary size distribution ranging from 100 to 375 nm, which was consistent with TEM observations. Zeta potential measurement showed a value of −18.7 mV, indicating negative surface charge and favorable stability (Figure S1). Furthermore, given

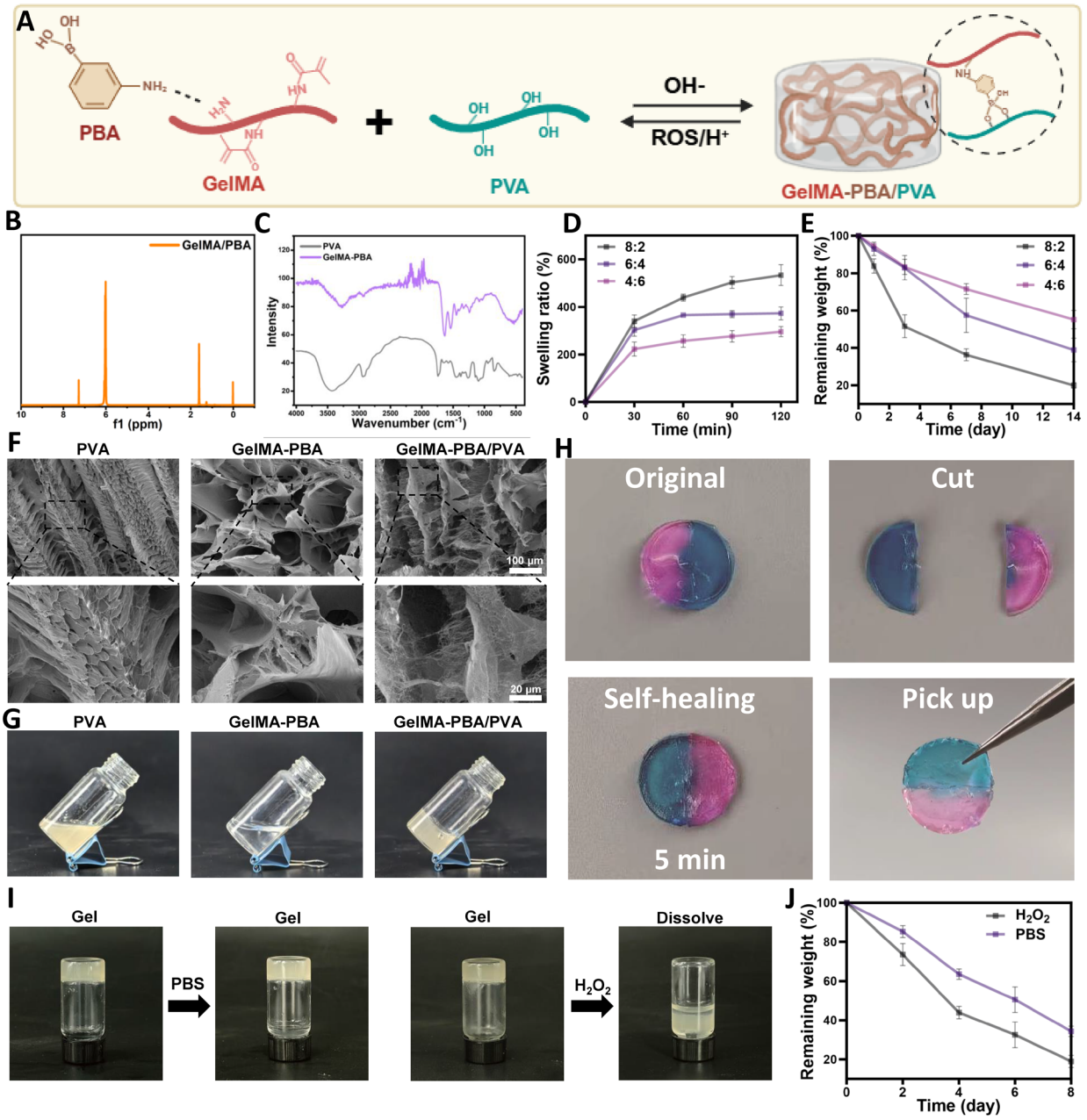

Figure 1. Synthesis, structural characterization, and functional properties of GPP hydrogel. (A) Schematic diagram of the construction of GelMA-PBA/PVA (GPP) hydrogel. (B) ^{1}H nuclear magnetic resonance (^{1}H NMR) spectrum of GPP hydrogel. (C) Fourier-transform infrared (FTIR) spectrum of GPP hydrogel. (D) Swelling ratio changes of GPP hydrogels with different GelMA-PBA/PVA ratios at various time points. (E) Mass loss rate of GPP hydrogels with different ratios at various time points. (F) SEM images of GelMA-PBA, PVA, and GPP hydrogels. (G) Gelation behavior of GPP hydrogel. (H) Self-healing performance of GPP hydrogel. (I) Reactive oxygen species (ROS) responsiveness of GPP hydrogel. (J) Mass loss rate changes of GPP hydrogel in ROS environments.

Abbreviations: GelMA: Methacrylated gelatin; PBA: Phenylboronic acid; PBS: Phosphate-buffered saline; PVA: Polyvinyl alcohol; ROS: Reactive oxygen species.

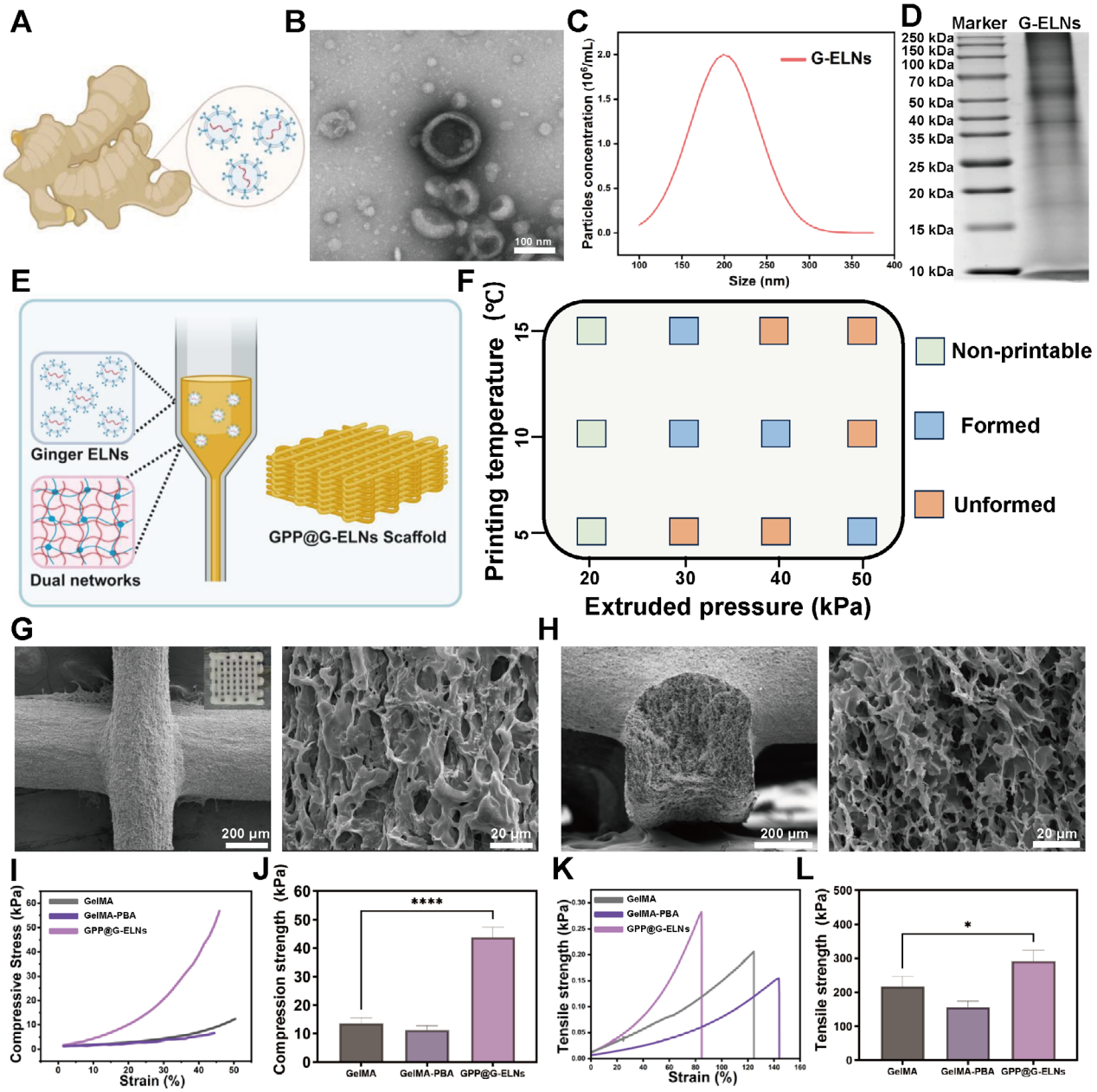

Figure 2. Construction and physicochemical characterization of the GPP@G-ELNs hydrogel scaffold. (A) Schematic illustration of the preparation process of G-ELNs. (B) Transmission electron microscopy (TEM) image of G-ELNs. (C) Particle size distribution analysis of G-ELNs by nanoparticle tracking analysis (NTA). (D) The distribution of proteins in G-ELNs was exhibited by Coomassie Brilliant Blue staining. (E) Schematic illustration of the fabrication of the 3D-printing GPP@G-ELNs hydrogel scaffold. (F) Evaluation of the extrusion performance of the printing ink. (G, H) Scanning electron microscopy (SEM) images of the surface and cross-section of the GPP@G-ELNs hydrogel scaffold. (I, J) Compressive stress–strain curves and compressive modulus of the GPP@G-ELNs hydrogel scaffold. (K, L) Tensile stress–strain curves and tensile strength of the GPP@G-ELNs hydrogel scaffold.
Notes: *$p < 0.05$, ****$p < 0.0001$; "ns" indicates no significant difference.
Abbreviations: GelMA: Methacrylated gelatin; PBA: Phenylboronic acid.

that proteins in plant-derived vesicles are crucial for their biological functions, we evaluated the protein composition of G-ELNs (Figure 2D). The results showed that G-ELNs exhibited particularly high protein abundance in the ranges of 100–250 kD, 35–70 kD, and 15–25 kD, suggesting the presence of a series of proteins that may contribute to their bioactivity. Subsequently, drug release assays were performed to assess the release efficiency of G-ELNs, which exhibited sustained release over 14 days, confirming their ability to continuously modulate the infectious

microenvironment (Figure S2).

The hydrogel scaffold (GPP@G-ELNs) with a well-defined porous architecture was fabricated using 3D printing technology, which facilitates the diffusion of oxygen and nutrients at the wound site (Figure 2E). The self-healing property of the GPP hydrogel enables it to maintain structural stability during the extrusion process, thereby ensuring good printability and shape fidelity of the scaffold. The extrusion performance of the hydrogel ink under different printing temperatures and extrusion pressures was further investigated (Figure 2F). The results indicated that optimal extrusion behavior was achieved when the printing temperature was maintained at 10 °C and the nozzle pressure was controlled within the range of 30–40 kPa. Based on these parameters, GPP@G-ELNs hydrogel scaffolds were successfully constructed on a low-temperature printing platform (Figure 2G and 2H). SEM images revealed that the scaffold exhibited a highly porous structure with pore sizes ranging from approximately 300 to 400 μm, which is conducive to cell infiltration and facilitates nutrient exchange and metabolic waste removal.

The mechanical properties of the scaffold were further systematically evaluated through tensile and compressive tests. The compressive stress–strain curves (Figure 2I and 2J) show that, compared with pure GelMA hydrogel (13.55 ± 1.67 kPa), the GelMA-PBA hydrogel exhibited a decrease in mechanical strength, which may be attributed to the introduction of PBA molecules partially interfering with the crosslinking density of the GelMA network, thereby reducing the overall mechanical integrity. In contrast, the GPP double-network hydrogel, constructed via physical crosslinking with PVA, displayed significantly enhanced mechanical strength (43.76 ± 2.96 kPa), indicating that the PVA network effectively reinforced the overall hydrogel network and improved its elasticity. Tensile stress–strain tests further confirmed this trend: the tensile strength of GPP hydrogel (290.15 ± 33.15 kPa) was markedly higher than that of GelMA hydrogel (218.67 ± 21.01 kPa) (Figure 2K and 2L). This superior mechanical performance not only ensures good compatibility and structural integrity with the surrounding tissue but also demonstrates the promising potential of this scaffold for applications in skin tissue engineering.[25]

3.4. *In vitro* biocompatibility evaluation of GPP@G-ELNs hydrogel

Good biocompatibility is a prerequisite for scaffolds used in wound repair.[26] We first evaluated the blood compatibility of the hydrogels using a hemolysis assay (Figure S3). The results showed that treatment with H_2O caused obvious red blood cell rupture and pronounced hemolysis, whereas no noticeable hemolytic behavior was observed in the solutions treated with GPP or GPP@G-ELNs, indicating their good blood compatibility. Furthermore, Live/Dead cell staining revealed that at both day 1 and day 3, no apparent dead cell signals (red fluorescence) were detected in the control, GPP, or GPP@G-ELNs groups, demonstrating that L929 cells maintained good viability during this period (Figure 3A).

Cell viability was further assessed using the CCK-8 assay. The results showed that after co-culture of L929 cells with the hydrogel extracts, cell viability in all groups remained above 95% (Figure 3B), further confirming the excellent biocompatibility of the GPP@G-ELNs scaffold and its suitability for subsequent *in vivo* evaluation. In addition, the EdU assay was employed to evaluate the effect of the hydrogels on cell proliferation (Figure 3C). The results demonstrated that the control, GPP, and GPP@G-ELNs groups all promoted cell proliferation to a certain extent, and quantitative analysis revealed that the GPP@G-ELNs group exhibited the most pronounced pro-proliferative effect (Figure 3D), which may be attributed to the sustained release of G-ELNs, thereby providing a potential advantage for its *in vivo* application.

3.5. *In vitro* antibacterial activity and promotion of macrophage polarization by GPP@G-ELNs hydrogel

Infectious wounds are typically accompanied by extensive bacterial colonization and an imbalanced immune microenvironment.[27]. Among them, *E. coli* and *S. aureus*, as the most common Gram-negative and Gram-positive bacteria, respectively, are the major pathogens responsible for persistent wound infections. To evaluate the antibacterial performance of the hydrogel system, Live/Dead fluorescence staining was employed to analyze both bacterial strains. As shown in Figure 4A, abundant green fluorescence signals were observed in the control and GPP groups, indicating high bacterial viability. In contrast, extensive red fluorescence was observed in the GPP@G-ELNs group for both *E. coli* and *S. aureus*, suggesting significant bacterial death and demonstrating the excellent antibacterial activity of the GPP@G-ELNs hydrogel. Further quantitative analysis of antibacterial efficiency revealed that GPP@G-ELNs achieved inhibition rates of approximately 71.01 ± 2.78% against *S. aureus* and 87.43 ± 3.72% against *E. coli* (Figure 4B and 4C), indicating its strong potential for *in vivo* antibacterial applications.

Persistent bacterial infection often leads to dysregulation of the immune microenvironment, which severely impedes wound healing.[28] As key regulators of the immune response, macrophages tend to accumulate in a pro-inflammatory M1 phenotype under inflammatory conditions. To investigate

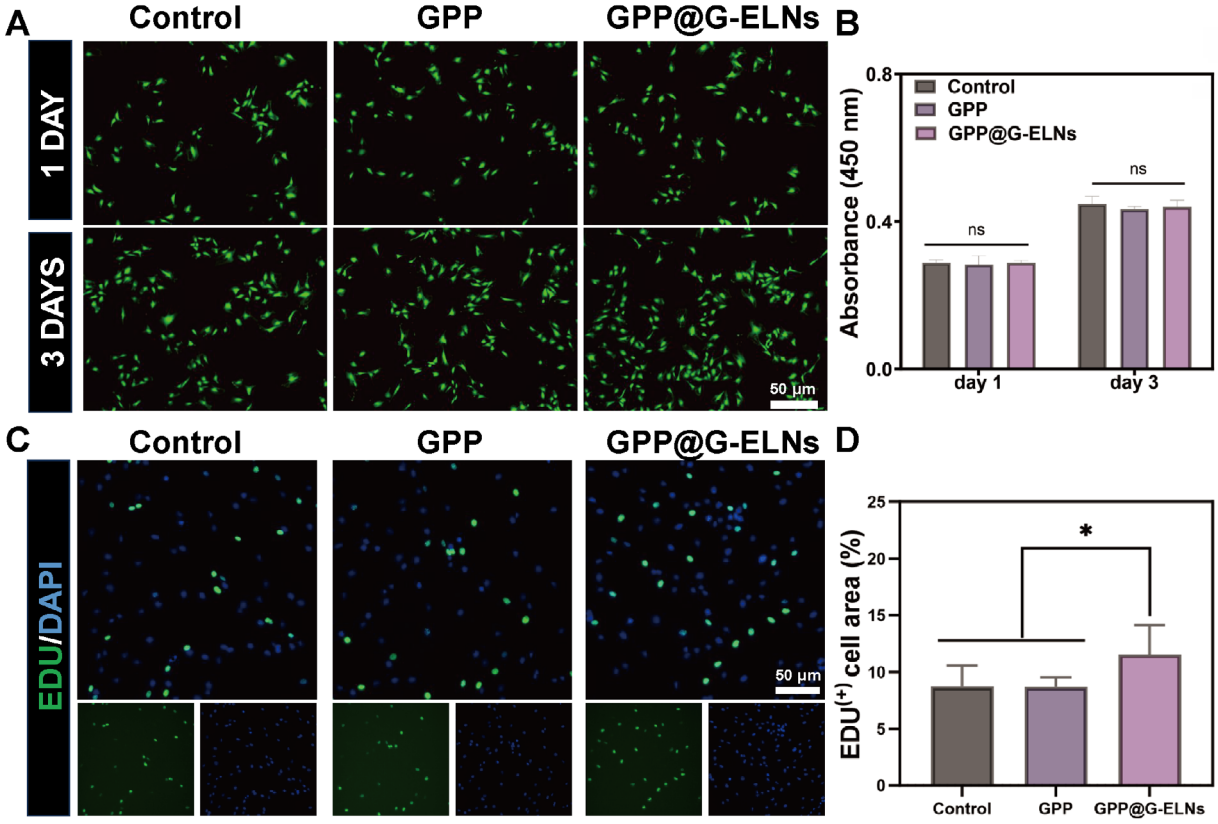

Figure 3. Biocompatibility evaluation of the GPP@G-ELNs hydrogel. (A) Representative Live/Dead fluorescence staining images of L929 cells after co-culture with GPP@G-ELNs hydrogel extracts for 1 and 3 days. (B) CCK-8 analysis of L929 cells after co-culture with GPP@G-ELNs hydrogel extracts for 1 and 3 days. (C, D) Representative EdU fluorescence staining images and quantitative analysis of L929 cells after co-culture with GPP@G-ELNs hydrogel extracts.
Notes: *$p < 0.05$; "ns" indicates no significant difference.

whether the GPP@G-ELNs hydrogel could modulate the inflammatory microenvironment, immunofluorescence staining was performed to analyze the M1 macrophage marker CD86 (Figure 4D). The results showed that macrophages stimulated with lipopolysaccharide (LPS) exhibited strong CD86 fluorescence, indicating high expression of pro-inflammatory markers. Similarly, strong CD86 expression was observed in the GPP-treated group, suggesting limited anti-inflammatory regulatory capacity. In contrast, macrophages treated with GPP@G-ELNs in the presence of LPS showed a significant reduction in CD86 expression, indicating that this hydrogel system effectively suppressed inflammation-related signaling. Furthermore, the expression of the M2 macrophage marker CD206 was examined. Macrophages in the LPS-stimulated and GPP-treated groups exhibited minimal CD206 expression, indicating persistent inflammation, whereas GPP@G-ELNs treatment significantly increased CD206 expression, promoting macrophage polarization toward the M2 phenotype (Figure 4E). Quantitative analysis of fluorescence intensity was consistent with these observations (Figure 4F and 4G). In addition, qPCR analysis of M1 markers IL-6 and TNF-α, as well as the M2 marker IL-10 (Figure 4H), confirmed that GPP@G-ELNs inhibited M1 macrophage expression while promoting M2 polarization. Collectively, these results demonstrate that GPP@G-ELNs hydrogel effectively induces macrophage polarization toward an anti-inflammatory, pro-repair phenotype, thereby actively modulating the immune microenvironment. This further supports that the GPP@G-ELNs hydrogel possesses both antimicrobial activity and immunomodulatory function in the context of infected wound healing.

3.6. Regulatory effect of the GPP@G-ELNs scaffold on wound healing

To investigate the regulatory effect of the GPP@G-ELNs

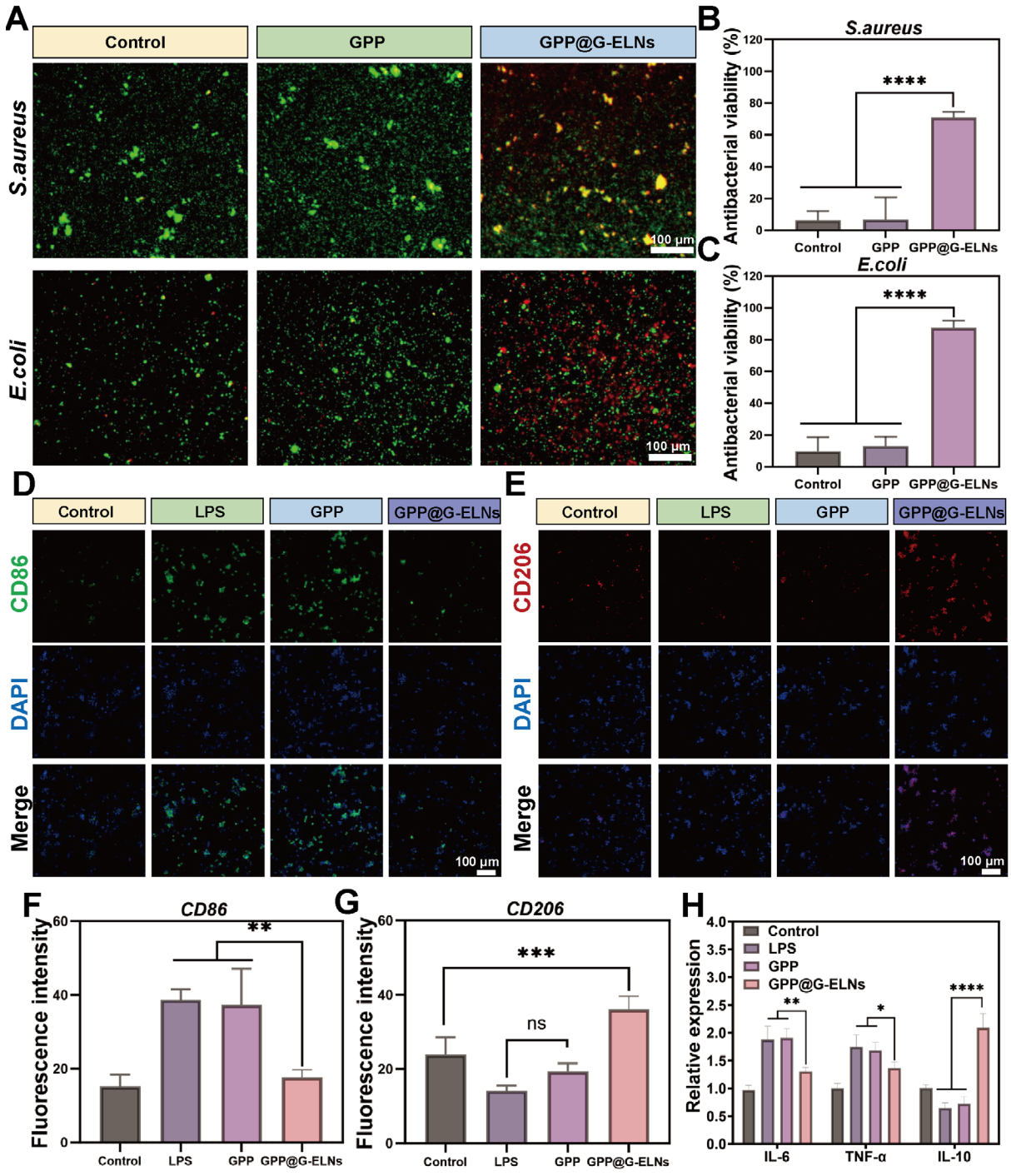

Figure 4. Antibacterial performance of the GPP@G-ELNs scaffold and its regulatory effect on macrophage polarization. (A) Live/Dead fluorescence staining images of *S. aureus* and *E. coli* after co-culture with the GPP@G-ELNs scaffold. (B) Inhibition rate of the GPP@G-ELNs scaffold against *S. aureus*. (C) Inhibition rate of the GPP@G-ELNs scaffold against *E. coli*. (D) Immunofluorescence staining images of the CD86 marker in macrophages pre-stimulated with LPS after co-culture with the GPP@G-ELNs scaffold. (E) Immunofluorescence staining images of the CD206 marker in macrophages pre-stimulated with LPS after co-culture with the GPP@G-ELNs scaffold. (F) Quantitative analysis of CD86 fluorescence intensity in different treatment groups. (G) Quantitative analysis of CD206 fluorescence intensity in different treatment groups. (H) Detection of IL-6, IL-10 and TNF-α expression after macrophage co-culture by PCR.

Notes: *$p < 0.05$, **$p < 0.01$, ***$p < 0.001$, ****$p < 0.0001$; "ns" indicates no significant difference.

Abbreviations: IL: Interleukin; LPS: Lipopolysaccharide; PCR: Polymerase chain reaction; TNF-α: Tumor necrosis factor alpha.

scaffold on wound healing, an infectious full-thickness skin wound model was first established on the backs of SD rats, and the healing process was evaluated through gross observation and histological analysis (Figure 5A). Figure 5B presents the wound healing progression of the control, GPP, and GPP@G-ELNs groups, along with quantitative analysis of wound closure. By day 7, the wound healing rates in the GPP and GPP@G-ELNs groups were significantly higher than those in the control group, with the GPP@G-ELNs group exhibiting the most pronounced improvement. By day 14, the GPP@G-ELNs group achieved nearly complete wound closure, whereas large unhealed areas remained in both the control and GPP groups.

Further quantitative analysis of wound area and healing rate (Figure 5C and 5D) revealed that on day 14, the wound area in the GPP@G-ELNs group was only 0.0592 ± 0.0079 cm², compared with 0.3966 ± 0.0151 cm² and 0.2818 ± 0.0069 cm² in the control and GPP groups, respectively. Correspondingly, the wound healing rate in the GPP@G-ELNs group reached $92.46 \pm 1.00\%$, which was markedly higher than that in the control group ($49.50 \pm 1.92\%$) and the GPP group ($64.13 \pm 0.87\%$). These results demonstrate that the GPP@G-ELNs hydrogel scaffold significantly accelerates wound healing and promotes tissue regeneration. Overall, the GPP@G-ELNs hydrogel effectively coordinates multiple phases of the healing process, including immunomodulation, angiogenesis, and extracellular matrix remodeling, thereby overcoming the pathological barriers of wounds and substantially improving repair quality and functional recovery.

Histological staining was performed on skin tissues harvested from SD rats on day 14 post-operation. As shown by H&E staining (Figure 5E), preliminary granulation tissue formation was observed in all groups; however, the control and GPP groups exhibited pronounced inflammatory cell infiltration, which is likely associated with persistent infection-induced inflammation at the wound site (Figure 5G). In contrast, abundant and actively proliferating fibroblasts were observed in the GPP@G-ELNs group, indicating a significant pro-healing effect of the GPP@G-ELNs hydrogel. Masson's trichrome staining further revealed that newly formed collagen fibers in the control group were sparsely distributed, whereas the GPP@G-ELNs group exhibited dense and well-organized collagen deposition, suggesting that the wound had progressed into the tissue remodeling stage. Immunohistochemical analysis further demonstrated that the GPP@G-ELNs hydrogel significantly downregulated the expression of inflammatory cytokines such as TNF-α, confirming its immunomodulatory capability (Figure 5F). Meanwhile, VEGF staining showed a markedly higher number of positive cells in the GPP@G-ELNs group compared with the control and GPP groups, further verifying its strong pro-angiogenic effect. Quantitative statistical analysis showed a consistent trend (Figure 5H and 5I). At the same time, we observed the COL-1 positive regions and found that GPP@G-ELNs significantly promoted the enrichment of COL-1 in the defect area, which is consistent with the results of Masson's trichrome staining (Figure S4).

4. Conclusion

In this study, we successfully developed a 3D-printed hydrogel scaffold (GPP@G-ELNs) loaded with ginger-derived exosome-like nanovesicles (G-ELNs) and validated its therapeutic efficacy for infectious wound repair. The scaffold can adapt to the dynamic wound microenvironment, maintain structural stability during the repair process, and exert responsive therapeutic effects to promote wound regeneration.

In the infectious full-thickness wound model, the GPP@G-ELNs hydrogel significantly accelerated wound closure, with excellent antibacterial, anti-inflammatory and pro-angiogenic activities. Histological evaluation confirmed that the scaffold markedly reduced inflammatory cell infiltration, promoted granulation tissue formation, and enhanced collagen deposition and remodeling. The core mechanism of its superior regenerative performance lies in the loading of G-ELNs, which modulates the local immune microenvironment of the wound, thereby synergistically enhancing the antibacterial efficacy and tissue regeneration capacity of the scaffold.

Nevertheless, several limitations of this study should be acknowledged. First, although the GPP@G-ELNs hydrogel showed promising therapeutic outcomes in animal models, further preclinical studies are required to validate its adaptability and efficacy across different types of wounds. Second, the source and extraction process of G-Exo may influence their biological activity and stability, necessitating additional optimization to ensure batch-to-batch consistency. Moreover, the long-term performance of the hydrogel, including its degradation behavior and potential long-term immune responses, was not investigated in this study and warrants further exploration, as these factors may impact its future clinical translation.

Acknowledgments

Not applicable.

Funding

This work was supported by the Chongqing Natural Science Foundation General Project under Grant CSTB2024NSCQ-MSX0921. Scientific Research Project of the Fuling District of Chongqing under Grant 2024AAN3057.

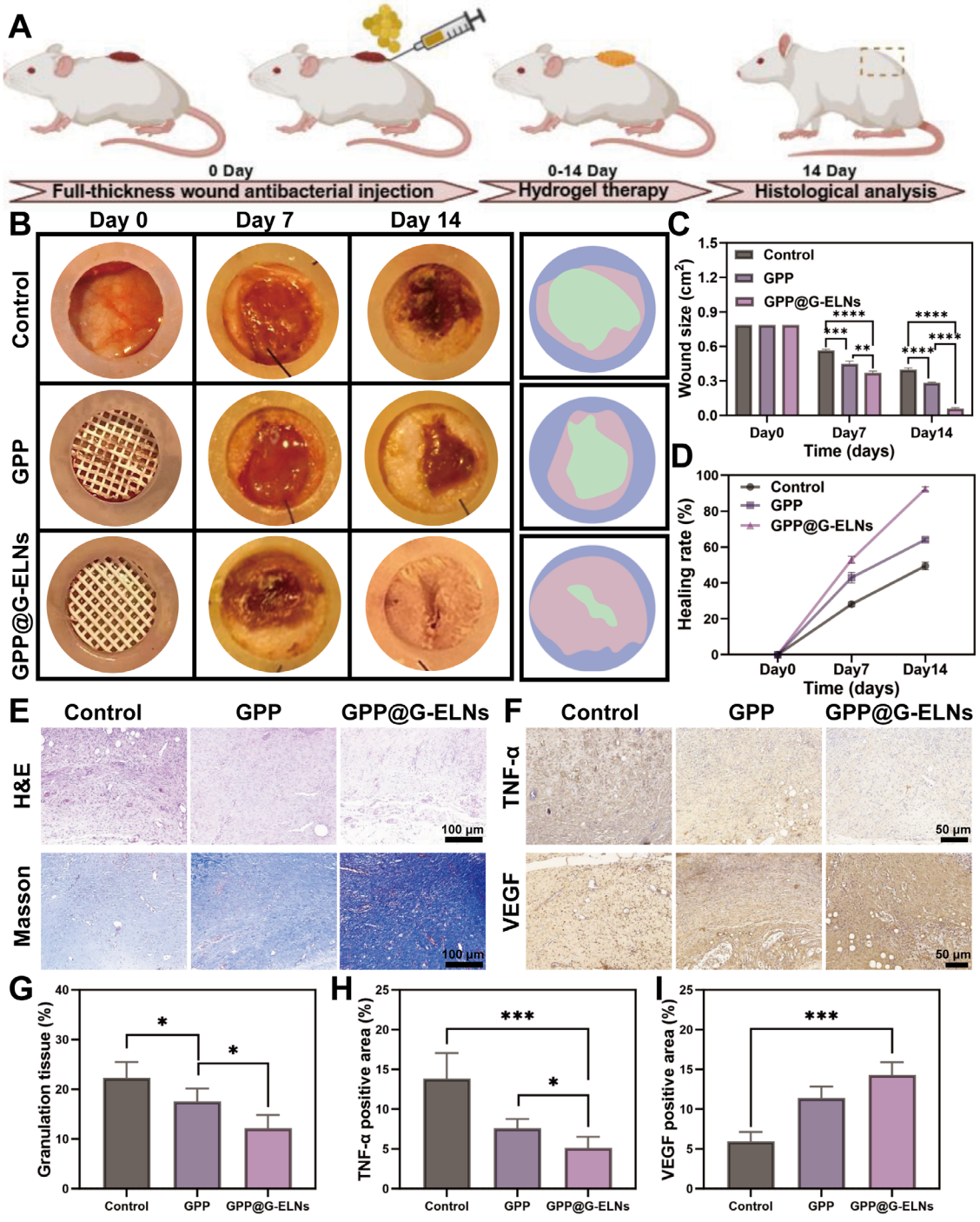

Figure 5. Regulatory effects of the GPP@G-ELNs scaffold on *in vivo* infectious wound healing. (A) Schematic illustration of the experimental procedure used to evaluate the effects of the GPP@G-ELNs scaffold on infectious wound healing in rats. (B) Representative photographs and schematic images showing the wound healing process in rats from different treatment groups. (C) Quantitative analysis of wound area in each group. (D) Quantitative analysis of wound healing rate in each group. (E) Hematoxylin and eosin (H&E) staining and Masson's trichrome staining images of wound skin tissues after 14 days of treatment. (F) Immunohistochemical staining images of TNF-α and VEGF in wound skin tissues after 14 days of treatment. (G) Quantitative analysis of newly formed granulation tissue in wound tissues after 14 days of treatment. (H, I) Quantitative statistical analysis of TNF-α- and VEGF-positive staining areas.

Notes: *$p < 0.05$, **$p < 0.01$, ***$p < 0.001$, ****$p < 0.0001$.

Abbreviations: TNF-α: Tumor necrosis factor alpha; VEGF: Vascular endothelial growth factor.

Conflict of interest

The authors declare no conflicts of interest.

Author contributions

Conceptualization: Shuhao Yang, Yidong Shen
Data curation: Yingying Chen
Formal analysis: Jixin Zhou
Funding acquisition: Jiayu Liu, Yixuan Lan, Kaichen Shen
Investigation: Shuhao Yang, Yidong Shen
Methodology: Haoming Wu
Project administration: Wei Huang, Leilei Qin
Supervision: Hai Wang
Writing–original draft: Shuhao Yang
Writing–review & editing: Shuhao Yang

Ethics approval and consent to participate

All animal experiments were conducted in accordance with the "Regulations on the Administration of Laboratory Animals" issued by the Ministry of Health of the People's Republic of China and were approved by the Ethics Committee of Chongqing Medical University (IACUC-CQMU-2025-0417).

Consent for publication

Not applicable.

Availability of data

Data are available from the corresponding author upon reasonable request.

References

1. Tan X, Lin N, Yang S, *et al.* AuCu@CuO_2 Aerogels with H_2O_2/O_2 Self-Supplying and Quadruple Enzyme-Like Activity for MRSA-Infected Diabetic Wound Management. *Adv Sci*. 2025;12(27):e2502391.

   doi: 10.1002/advs.202502391

2. Uberoi A, McCready-Vangi A, Grice EA. The wound microbiota: microbial mechanisms of impaired wound healing and infection. *Nat Rev Microbiol.* 2024;22(8):507-521.

   doi: 10.1038/s41579-024-01035-z

3. Wang X, Dong J, Kang J, *et al.* Self-Adaptive Release of Stem Cell-Derived Exosomes from a Multifunctional Hydrogel for Accelerating MRSA-Infected Diabetic Wound Repair. *J Am Chem Soc.* 2025;147(19):16362-16378.

   doi: 10.1021/jacs.5c02184

4. Chen G, Wu H, Zhao X, *et al.* Drug-Loaded Janus Dressings Precipitated from PEG–PTMC Thermosensitive Hydrogel for Oral Ulcer Treatment. *Chem Mater*. 2025;37(5):1865-1880.

   doi: 10.1021/acs.chemmater.4c03077

5. Lai CM, Chen WJ, Qin Y, Xu D, Lai YK, He SH. Innovative hydrogel design: tailoring immunomodulation for optimal chronic wound recovery. *Adv Sci*. 2025;12(2):2412360.

   doi: 10.1002/ADVS.202412360

6. Fang Y, Han Y, Yang L, *et al.* Conductive hydrogels: intelligent dressings for monitoring and healing chronic wounds. *Regen Biomater*. 2025;12:rbae127.

   doi: 10.1093/rb/rbae127

7. Gan S, Zheng Z, Li X, *et al.* Scab-Inspired Thermoresponsive Hydrogel Dressing for Accelerated Healing of Infected Wounds. *ACS Appl Mater Interfaces*. 2026.

   doi: 10.1021/acsami.5c21571

8. Xiang T, Guo Q, Jia L, *et al.* Multifunctional hydrogels for the healing of diabetic wounds. *Adv Healthc Mater.* 2024;13(1):2301885.

   doi: 10.1002/adhm.202301885

9. Lin X, Zhang X, Wang Y, Chen W, Zhu Z, Wang S. Hydrogels and hydrogel-based drug delivery systems for promoting refractory wound healing: Applications and prospects. *Int J Biol Macromol.* 2025;285:138098.

   doi: 10.1016/j.ijbiomac.2024.138098

10. Lu Z, Tan K, Xiang S, *et al.* Peptide loaded self-healing hydrogel promotes diabetic skin wound healing through macrophage orchestration and inflammation inhibition. *Mater Today Bio*. 2025;32:101690.

    doi: 10.1016/j.mtbio.2025.101690

11. Tan Y, Xu C, Liu Y, Bai Y, Li X, Wang X. Sprayable and self-healing chitosan-based hydrogels for promoting healing of infected wound via anti-bacteria, anti-inflammation and angiogenesis. *Carbohydr Polym*. 2024;337:122147.

    doi: 10.1016/j.carbpol.2024.122147

12. Gao S, Chen T, Deng C, Liu G, Wei Z. An endoplasmic reticulum stress-responsive nanocomposite hydrogel for diabetic wound healing through a fibroblast-immune cell dual regulation hub. *J Nanobiotechnol*. 2025;23(1):689.

    doi: 10.1186/s12951-025-03732-0

13. Zhang F, Zhang H, Wang S, *et al.* A dynamically phase-adaptive regulating hydrogel promotes ultrafast anti-fibrotic wound healing. *Nat Comm*. 2025;16(1):3738.

    doi: 10.1038/s41467-025-58987-w

14. Xu R, Ooi HS, Bian L, Ouyang L, Sun W. Dynamic hydrogels for biofabrication: A review. *Biomaterials*. 2025:320.

    doi: 10.1016/j.biomaterials.2025.123266

15. Zhou X, Yu X, You T, *et al.* 3D printing-based hydrogel dressings for wound healing. *Adv Sci*. 2024;11(47):2404580.

doi: 10.1002/advs.202404580

16. Cao W, Peng S, Yao Y, *et al*. A nanofibrous membrane loaded with doxycycline and printed with conductive hydrogel strips promotes diabetic wound healing in vivo. *Acta Biomater*. 2022;152:60-73.

doi: 10.1016/j.actbio.2022.08.048

17. Zhu J, Zeng Q, Liu Y, *et al*. Smart nanosilver strikes twice: precision bacteria killing meets autophagy-boosted healing for infected wounds. *Adv Funct Mater*. 2025;35(48):2507797.

doi: 10.1002/adfm.202507797

18. Gong L, Chang L, Chen S, *et al*. Multifunctional injectable hydrogel with self-supplied H(2)S release and bacterial inhibition for the wound healing with enhanced macrophages polarization via interfering with PI3K/Akt pathway. *Biomaterials*. 2025;318:123144.

doi: 10.1016/j.biomaterials.2025.123144

19. Wang S, Zhang Y, Zeng Y, *et al*. Plant-derived vesicle-like nanoparticles for immunomodulation: Mechanisms and applications. *Bioact Mater*. 2026;55:171-204.

doi: 10.1016/J.BioActmat.2025.09.024

20. Han R, Zhou D, Ji N, *et al*. Folic acid-modified ginger-derived extracellular vesicles for targeted treatment of rheumatoid arthritis by remodeling immune microenvironment via the PI3K-AKT pathway. *J Nanobiotechnol*. 2025;23(1):41.

doi: 10.1186/S12951-025-03096-5

21. Mu N, Li J, Zeng L, *et al*. Plant-Derived Exosome-Like Nanovesicles: Current Progress and Prospects. *Int J Nanomed*. 2023;18:4987-5009.

doi: 10.2147/IJN.S420748

22. Li L, Wang F, Zhu D, Hu S, Cheng K, Li Z. Engineering exosomes and exosome-like nanovesicles for improving tissue targeting and retention. *Fundam Res*. 2025;5(2):851-867.

23. Li D, Que N, Tang H, *et al*. Advances in Hydrogel-Based Electronic Skins: From Material Design to Multifunctional Applications. *Adv Funct Mater*. 2025:e27525.

doi: 10.1002/adfm.202527525

24. Terriac L, Helesbeux J-J, Maugars Y, Guicheux J, Tibbitt MW, Delplace V. Boronate ester hydrogels for biomedical applications: challenges and opportunities. *Chem Mater*. 2024;36(14):6674-6695.

doi: 10.1021/acs.chemmater.4c00507

25. Jiang L, Dong J, Jiang M, *et al*. 3D-printed multifunctional bilayer scaffold with sustained release of apoptotic extracellular vesicles and antibacterial coacervates for enhanced wound healing. *Biomaterials*. 2025;318:123196.

doi: 10.1016/j.biomaterials.2025.123196

26. Wang Y, Gao C, Cheng S, *et al*. 3D Bioprinting of Double-Layer Conductive Skin for Wound Healing. *Adv Healthc Mater*. 2025;14(9):2404388.

doi: 10.1002/adhm.202404388

27. Fan Y-L, Liu H-J, Wang Z-L, *et al*. A one-nano MOF-two-functions strategy toward self-healing, anti-inflammatory, and antibacterial hydrogels for infected wound repair. *Chem Eng J*. 2024;497:155037.

doi: 10.1016/j.cej.2024.155037

28. Xu H, Zhao X, Wang J, *et al*. A glucose-activated cascade oxygen release hydrogel wound dressing for microenvironment regulation of MRSA-infected diabetic wounds. *Nano Today*. 2026;67:102962.

doi: 10.1016/j.nantod.2025.102962